Supplementary Materials: Dynamic Mapping of Evapotranspiration Using an Energy Balance-Based Model over an Andean Páramo Catchment of Southern Ecuador

Galo Carrillo-Rojas, Brenner Silva, Mario Córdova, Rolando Célleri and Jörg Bendix

1. METRIC$_L$ and METRIC$_M$ Implementation Flowchart

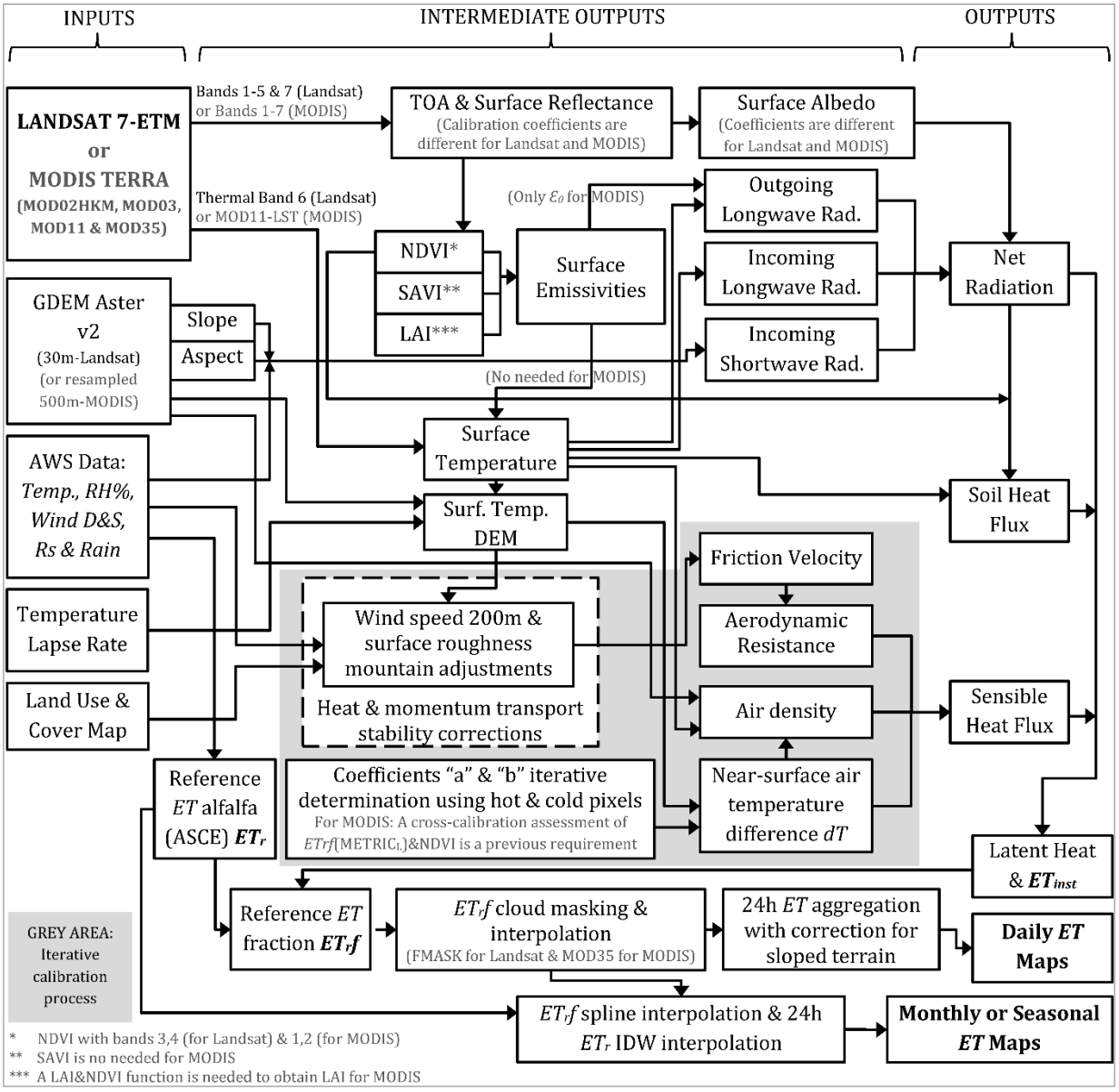

Figure S1. METRIC$_L$ and METRIC$_M$ algorithms flowchart (adapted from equations of Allen *et al.* [1] and Trezza *et al.* [2]).

2. Abbreviations

Table S1. Abbreviations used in this supplementary information (Equations (S1)–(S32)).

Abbreviation	Full Name	Units
ET	Evapotranspiration	mm
LE	Latent heat flux	W·m^{-2}
R_N	Net radiation	W·m^{-2}
G	Soil heat flux	W·m^{-2}
H	Sensible heat flux	W·m^{-2}
$R_{S,in}$	Incoming shortwave radiation	W·m^{-2}
$R_{L,in}$	Incoming longwave thermal radiation from the atmosphere	W·m^{-2}
$R_{L,out}$	Outgoing longwave thermal radiation	W·m^{-2}
ε_0	Broad-band surface emissivity	dimensionless
T_s	Temperature of the surface	K
LAI	Leaf Area Index	m^2·m^{-2}
$SAVI$	Soil Adjusted Vegetation Index	dimensionless
$NDVI$	Normalized Difference Vegetation Index	dimensionless
r_{ah}	Aerodynamic resistance to heat transfer	s·m^{-1}
dT	Near surface temperature difference	K
AWSs	Automatic weather stations	-
u^*	Friction velocity	m·s^{-1}
u_{200}	Wind speed at a blending height (200 m)	m·s^{-1}
z_{om}	Momentum roughness length	m
$z_{om(mtn)}$	Mountain adjusted roughness length	m
ϖ	Wind speed weighting coefficient	dimensionless
T_{sDEM}	Lapse rate corrected surface temperature	K
L	Monin-Obukhov Length	m
ET_r	ASCE-ERWI Standardized Reference Evapotranspiration for alfalfa	mm·h^{-1}
ET_{inst}	Instantaneous actual ET	mm·h^{-1}
λ	Latent heat of vaporization of water	J·kg^{-1}
ET_rf	Reference Evapotranspiration fraction (crop coefficient at reference alfalfa basis)	dimensionless
ET_{day}	ET at a daily basis (24 h)	mm·day^{-1}
K_c	Grass-based crop coefficient	dimensionless
K_{ratio}	Conversion value for ET_rf to K_c	dimensionless

3. Description of the METRIC Landsat-Based Implementation

According to the methodology of Allen *et al.* [1] METRIC delivers the instantaneous latent heat flux (LE) on a pixel-by-pixel basis as a residual of the energy balance Equation (S1):

$$LE = R_N - G - H \quad (\mathrm{W \cdot m^{-2}}) \tag{S1}$$

Here LE can be expressed as actual evapotranspiration ET by dividing it by the latent heat of vaporization. We calculated R_N considering: $R_{S,in}$, the outgoing shortwave radiation retrieved by multiplying $R_{S,in}$ with Albedo (α), $R_{L,in}$, $R_{L,out}$, and ε_0. Equation (S2) describes this calculation.

$$R_N = R_{S,in} - \alpha \times R_{S,in} + R_{L,in} - R_{L,out} - (1 - \varepsilon_0) \times R_{L,in} \quad (\mathrm{W \cdot m^{-2}}) \tag{S2}$$

$R_{S,in}$ was calculated using Equation (S3).

$$R_{S,in} = \frac{G_{sc} \times \mathrm{Cos}\theta_{rel} \times \tau_{sw}}{d^2} \quad (\mathrm{W \cdot m^{-2}}) \tag{S3}$$

where G_{sc} is the solar constant (1367 W·m^2), Cosθ considers the slope and aspect terrain adjustments according [1,3]. τ_{sw} is the atmospheric transmissivity obtained with the ASCE-ERWI method [4], and d^2 is the square of the relative earth-sun distance at the day of the image. α was calculated by integrating satellite spectral reflectance values from bands 1 to 5 and 7 of Landsat image according [5]. $R_{L,out}$ was calculated using the Stephan-Boltzmann equation (Equation (S4)).

$$R_{L,out} = \sigma \times \varepsilon_0 \times T_s^4 \quad (\mathrm{W \cdot m^{-2}}) \tag{S4}$$

where σ is the Stephan-Boltzmann constant (5.67 × 10^{-8} W·m^{-2}·K^{-4}). ε_0 was computed using an empirical equation developed by Tasumi [6] (Equation (S5)).

$$\varepsilon_0 = 0.95 + 0.01 \times LAI \quad \text{for } LAI \leq 3 \tag{S5}$$

The equation is limited to ε_0 = 0.98 when $LAI > 3$. LAI was computed using the equation from Bastiaanssen [7] (Equation (S6)).

$$LAI = -\frac{\ln(\frac{0.69 - SAVI}{0.59})}{0.91} \tag{S6}$$

$SAVI$ considers the top-of-atmosphere reflectance bands number 3 and 4 of the images (Equation (S7)).

$$SAVI = \frac{(1 - L_{const}) \times (\rho_{\lambda,4} - \rho_{\lambda,3})}{(\rho_{\lambda,4} + \rho_{\lambda,3})} \tag{S7}$$

L_{const} constant value represents the soil-brightness dependent factor. We calibrated L_{const} for our study area and a value of 0.05 was found after processing the images according to the method recommended by Huete [8]. T_s was estimated for Landsat imagery using the methodology proposed by Markham and Barker [9] which accounts for emissivity and atmospheric specific corrections (Equation (S8)).

$$T_s = \frac{K_2}{\ln[\left(\varepsilon_{NB} \times \frac{K_1}{L_{C\lambda,6}}\right) + 1]} \quad (\mathrm{K}) \tag{S8}$$

Here, K_1 and K_2 constants were 666.09 and 1282.71 W·m^{-2}·sr^{-1} respectively for Landsat, and the corrected thermal radiance $L_{C\lambda,6}$ was calculated using the approach from Wukelic *et al.* [10]. In this calculation we applied the default values recommended by Allen *et al.* [1] for the path radiance ($R_p = 0$), downward thermal radiation from clear sky ($R_{sky} = 0$), and narrow band transmissivity or air ($\tau_{NB} = 1$) due to the lack of radio sounding data for the study area.

The T_s was internally adjusted during the creation of the dT function according Allen *et al* [1]. The narrow-band surface emissivity (ε_{NB}) was calculated using the approach from Tasumi [6] similarly to ε_0. The $R_{L,in}$ was calculated by Equation (S9).

$$R_{L,in} = \sigma \times \varepsilon_a \times T_a^4 \quad (\mathrm{W \cdot m^{-2}}) \tag{S9}$$

where ε_a is the effective atmospheric emissivity and T_a is the air temperature. The ε_a was obtained according Allen *et al.* [1] and Bastiaanssen [11]. METRIC applications generally use T_s as a surrogate of T_a in the calculation of $R_{L,out}$ and $R_{L,in}$. This assumption was appropriate considering the high altitude and predominant wet conditions of the Andean páramo, where differences between the surface and near-surface air temperatures tends to be small [1]. G in W·m^{-2} was calculated using the approach of Bastiaanssen *et al.* [12] (Equation (S10)).

$$G = (T_s - 273.15) \times (0.0038 + 0.0074 \times \alpha) \times (1 - 0.98 \times NDVI^4) \times R_N \tag{S10}$$

This approach was considered because $NDVI$ input is more appropriate for heterogeneous terrain instead of LAI when estimating G [13]. The $NDVI$ was calculated according to Equation (S11).

$$NDVI = \frac{(\rho_{\lambda,4} - \rho_{\lambda,3})}{(\rho_{\lambda,4} + \rho_{\lambda,3})} \tag{S11}$$

where $\rho_{\lambda,4}$ and $\rho_{\lambda,4}$ are the Landsat reflectances from near-infrared and red bands respectively. We estimated H employing an aerodynamic function (Equation (S12)):

$$H = \rho_{air} \times C_p \times \frac{dT}{r_{ah}} \quad (\mathrm{W \cdot m^{-2}}) \tag{S12}$$

where ρ_{air} is the air density ($\mathrm{kg \cdot m^{-3}}$), C_p is the specific heat of air at constant pressure ($\mathrm{J \cdot kg^{-1} \cdot K^{-1}}$), r_{ah} in $\mathrm{s \cdot m^{-1}}$ was retrieved between two near surface heights z_1 = 0.1 m and z_1 = 2 m, and dT in Kelvin was retrieved similarly between z_1 and z_2. In Equation (S12) both r_{ah} and dT were unknown and required an iterative process to solve it.

The r_{ah} was calculated by extrapolating wind speed to some blending heights above the surface (usually 100 to 200 m) and corrected with an iterative stability scheme based on the Monin-Obukhov functions (Equation (S13)):

$$r_{ah} = \frac{\ln(\frac{z_1}{z_2})}{k \times u^*} \tag{S13}$$

k is Von Karman's constant (0.41). u^* in $\mathrm{m \cdot s^{-1}}$ was applied for neutral atmospheric conditions and was computed during the first iteration using Equation (S14).

$$u^* = \frac{k \times u_{200}}{\ln(\frac{200}{z_{om}})} \tag{S14}$$

The term u_{200} was calculated using Equation (S15).

$$u_{200} = \frac{u_{AWS} \times \ln(\frac{200}{z_{omAWS}})}{\ln(\frac{z_{AWS}}{z_{omAWS}})} \tag{S15}$$

In the equation, u_{AWS} is wind speed measured at z_{AWS} height (m) above the surface, and z_{omAWS} is the estimated roughness length (m) at the same place. To represent z_{om} we employ a land use and land cover map (LULC) where we assigned z_{om} values according to land use type and vegetation cover. The assigned z_{om} values were: Water (0.0005 m), páramo grasslands (0.020 m), páramo flooded grasslands (0.020 m), evergreen shrublands with grasslands (0.125 m), high montane evergreen forest (0.20 m) and inter-Andean montane evergreen forest (0.25 m). These values were selected according to several studies [14–17].

To account for mountainous effects we implemented the empirical methodology recommended by Allen *et al.* [18] where an adjustment of z_{om} was applied using Equation (S16).

$$z_{om(mtn)} = z_{om} \times \left(1 + \frac{s_d - 5}{20}\right); \quad \text{for } s_d \geq 5 \tag{S16}$$

where s_d is the slope of each pixel in degrees. In the same way, the term u_{200} for mountainous image pixels was multiplied by a wind speed weighting coefficient (ϖ), before computations of $u^*$and r_{ah}. The function is on Equation (S17).

$$\varpi = 1 + 0.1 \times \left(\frac{E_{DEM} - E_{AWS}}{1000}\right) \tag{S17}$$

In this equation, E_{DEM} and E_{AWS} are the elevation of each pixel and elevation of the AWSs respectively. T_s was corrected using the difference in elevation in relation to an arbitrary point in the image where $T_{sDEM} = T_s$ according Allen *et al.* [18] (Equation (S18)).

$$T_{sDEM} = T_s - CT_{lr} \times \Delta z \tag{S18}$$

Specific calibration of the temperature lapse rate CT_{lr} was performed using the methodology proposed by Allen *et al.* [18] and was applied for each image date (CT_{lr} mean = 0.68 °C each 100 m).

During ten iterations corrected values for u^* were computed using Equation (S19). We choose this number of iterations to ensure that the change in r_{ah} is less than 0.1% at the end of the process.

$$u^* = \frac{k \times u_{200}}{\ln\left(\frac{200}{z_{om}}\right) - \Psi_{M(200)}} \quad \text{(S19)}$$

Herein, $\Psi_{m(200)}$ is the stability correction for momentum transport at 200 m. Then r_{ah} was recalculated using Equation (S20):

$$r_{ah} = \frac{\ln\left(\frac{z_1}{z_2}\right) - \Psi_{H(z_2)} + \Psi_{H(z_1)}}{k \times u^*} \quad \text{(S20)}$$

where $\Psi_{H(z_2)}$ and $\Psi_{H(z_1)}$ are stability corrections for the heat transport at heights z_2 & z_1. The terms $\Psi_{M(200)}$, $\Psi_{H(z_2)}$ and $\Psi_{H(z_1)}$ were updated in the iterative process following the approaches outlined by Paulson [19] and Webb [20], which employ the Monin-Obukhov length L defined by Equation (S21).

$$L = -\frac{\rho_{air} \times C_p \times u^{*3} \times T_s}{k \times g \times H} \quad \text{(S21)}$$

This function contemplates the variables mentioned above, and also the gravitational acceleration g (9.807 m·s^{-2}) and the air density ρ_{air} at the pixel elevation (kPa). A comprehensive explanation of this process is available in Allen *et al.* [1].

The dT function assumes a linear relationship with T_s where coefficients *a* and *b* were used to correct the function in an iterative computation.

$$dT = a + b \times T_s \quad \text{(S22)}$$

In Equation (S22) the *a* and *b* coefficients have an empirical determination based on two extreme conditions in the image. The named hot and cold pixels were selected by two specific criteria: the hot pixel was a relative dry, non-vegetated, and with higher temperature pixel, and the cold pixel was a wet and fully vegetated pixel, both located in the proximity of the three AWSs. The selection of these pixels for each image was based on a rigorous process of visual and software assisted selection of pixels in T_s, α, $NDVI$, LAI, and slope images. Most of the hot pixels were located on non- or sparsely-vegetated areas in the mid and high areas of the grasslands, and the wet pixels were mostly selected from the *Polylepis* sp. tree patches near wetlands. Temperature differences between the cold and hot pixels ranged in 5 to 7 °C for our study. Hence, the estimations for dT were assessed using Equations (S23) and (S24):

$$dT_{hot} = \frac{(R_N - G) \times r_{ah,hot}}{\rho_{air,hot} \times C_p} \quad \text{(S23)}$$

$$dT_{cold} = \frac{(R_N - G - 1.05 \times ET_r) \times r_{ah,cold}}{\rho_{air,cold} \times C_p} \quad \text{(S24)}$$

In the Equation (S24), an adjustment with the instantaneous ET_r obtained according the methodology of ASCE-ERWI [4] accounts for an increased condition of ET in the cold pixel (5% greater) [1]. The Equation (S25) calculates H for the hot and cold pixels.

$$H_{hot} = (R_N - G)_{hot} - LE_{hot} \;\; ; \;\; H_{cold} = (R_N - G)_{cold} - LE_{cold} \quad \text{(S25)}$$

At the end of the iterative process, *a* and *b* coefficients were determined using Equations (S26) and (S27).

$$a = \frac{dT_{hot} - dT_{cold}}{T_{sDEM,hot} - T_{sDEM,cold}} \quad \text{(S26)}$$

$$b = \frac{dT_{hot} - a}{T_{sDEM,hot}} \quad \text{(S27)}$$

where $T_{sDEM,hot}$ and $T_{sDEM,cold}$ are the lapse rate corrected surface temperatures for the hot and cold pixels. These two conditions tie the calculations for all pixels in the image.

Once R_N, H, and G were calculated, we applied the Equation (S1) to obtain LE as the residual of the balance. Hereafter, we divided LE by the λ to obtain the instantaneous actual ET (ET_{inst}) at the satellite image time. Equation (S28) describes this:

$$ET_{inst} = 3600 \frac{LE}{\lambda \times \rho_w} \quad (\text{mm} \cdot \text{h}^{-1}) \tag{S28}$$

where 3600 is the conversion from seconds to hours and ϱ_w is the density of water (1000 kg·m^{-3}). λ was calculated using the Equation (S29).

$$\lambda = [2.501 - 0.00236 \times (T_s - 273.15)] \times 10^6 \quad (\text{J} \cdot \text{kg}^{-1}) \tag{S29}$$

A requirement to convert hourly ET_{inst} into a daily basis is to obtain ET_rf. This variable was calculated dividing ET_{inst} by the ET_r (Equation (S30)). ET_rf is also the equivalent of the crop coefficient (*Kc*) when used with an alfalfa reference basis [1,4]. The advantage of this calibration via ET_r is that each pixel of the ET_rf image retains a unique value for ET_{inst} which can be interpolated in the time using representative dataset from the weather stations.

$$ET_rf = \frac{ET_{inst}}{ET_r} \tag{S30}$$

Prior to the calculation of daily evaporation the minor areas of the ET_rf images had to be masked to avoid contamination due to clouds [1,21,22]. This was done in two steps: (1) identification and masking of clouds and cloud-shadows (considering a buffer of 200 m surrounding the cloud/shadow) with the application of the FMASK algorithm proposed by Zhu and Woodcock [23] and (2) implementing the methodology recommended by Kjaersgaard *et al.* [24] which fills in the masked areas using a time weighted interpolation of the ET_rf values from the precedent and following satellite images containing valid ET_rf estimates. This method considers an adjustment for vegetation (using $NDVI$) to account for reflectance changes over the time.

Equation (S31) shows calculation of ET_{day}. It was obtained by multiplying ET_rf times hourly aggregated ET_r in 24-h periods times a correction term $C_{solar24}$ to account for the variation of solar radiation over sloping terrain in 24 h.

$$ET_{day} = ET_rf \times \sum_{i=1}^{24} ET_{r,(i)} \times C_{solar24} \quad (\text{mm} \cdot \text{day}^{-1}) \tag{S31}$$

$C_{solar24}$ was calculated using daily extraterrestrial and clear-sky solar energy using the methodology suggested by Allen *et al.* [25].

Monthly ET was calculated assuming that ET changes in proportion to the change in ET_r at the AWSs. Last, according to Kjaersgaard *et al.* [26], a cubic spline interpolation of the daily ET_rf maps over the study period was implemented, as well as an spatial inverse weighted interpolation (IDW) to recreate maps of ET_r using the information of the three AWSs in the same period.

4. The K_{ratio} Conversion Factor Methodology

According to the methodology of Allen *et al.* [26] a crop coefficient based on the alfalfa reference (in our case ET_rf) can be converted to a crop coefficient with a grass reference (K_c) by multiplying it by a conversion value (K_{ratio}) which usually ranges between 1.0 to 1.3. The Equation (S32) uses averaged climate data for the period of study and a constant value of the alfalfa crop coefficient for the mid-season stage ($K_{c\,mid}$):

$$K_{\text{ratio}} = K_{c\,mid} + [0.04 \times (u_{AWS\,mean} - 2) - 0.004 \times (RH_{min} - 45)] \times \left(\frac{h}{3}\right)^{0.3} \tag{S32}$$

Herein $K_{c\,mid}$ = 1.20 was obtained from tables in [27], $u_{AWS\,mean}$ was the daily mean value for wind speed during the study period, RH_{min} was the mean value for daily minimum relative humidity (%) during the study period, and h is the height for alfalfa reference crop (h = 0.5).

References

1. Allen, R.G.; Tasumi, M.; Trezza, R. Satellite-Based Energy Balance for Mapping Evapotranspiration with Internalized Calibration (METRIC)—Model. *J. Irrig. Drain. Eng.* **2007**, *133*, 380–394.
2. Trezza, R.; Allen, R.G.; Tasumi, M. Estimation of actual evapotranspiration along the Middle Rio Grande of New Mexico using MODIS and landsat imagery with the METRIC model. *Remote Sens.* **2013**, *5*, 5397–5423.
3. Duffie, J.A.; Beckman, W.A. *Solar Engineering of Thermal Processes*, 2nd ed.; Wiley Interscience: New York, NY, USA, 1991.
4. ASCE-EWRI. *The ASCE Standardized Reference Evapotranspiration Equation*; ASCE–EWRI Standardization of Reference Evapotranspiration Task Committe Report; ASCE: Reston, WV, USA, 2005.
5. Tasumi, M.; Allen, R.G.; Trezza, R. At-Surface Reflectance and Albedo from Satellite for Operational Calculation of Land Surface Energy Balance. *J. Hydrol. Eng.* **2008**, *13*, 51–63.
6. Tasumi, M. Progress in Operational Estimation of Regional Evapotranspiration Using Satellite Imagery. Ph.D. Thesis, University of Idaho, Moscow, ID, USA, 2003.
7. Bastiaanssen, W.G.M. *Remote Sensing in Water Resources Management: The State of the Art*; International Water Management Institute: Colombo, Sri Lanka, 1998.
8. Huete, A.R. A soil-adjusted vegetation index (SAVI). *Remote Sens. Environ.* **1988**, *25*, 295–309.
9. Markham, B.L.; Barker, J.L. Landsat MSS and TM post-calibration dynamic ranges, exoatmospheric reflectances and at-satellite temperatures. *EOSAT Landsat Tech. Notes* **1986**, *1*, 3–8.
10. Wukelic, G.E.; Gibbons, D.E.; Martucci, L.M.; Foote, H.P. Radiometric calibration of Landsat Thematic Mapper thermal band. *Remote Sens. Environ.* **1989**, *28*, 339–347.
11. Bastiaanssen, W.G.M. Regionalization of Surface Flux Densities and Moisture Indicators in Composite Terrain: A Remote Sensing Approach under Clear Skies in Mediterranean Climates. Ph.D. Thesis, University of Wageningen, Wageningen, The Netherlands, 1995.
12. SEBAL Remote Sensing Tool for Water Consumption. Available online: http://www.waterwatch.nl/publications/posters/the-sebal-remote-sensing-tool-for-water-consumption.html (accesson on 16 February 2016).
13. Cuenca, R.H.; Ciotti, S.P.; Hagimoto, Y. Application of landsat to evaluate effects of irrigation forbearance. *Remote Sens.* **2013**, *5*, 3776–3802.
14. Hansen, F.V. *Surface Roughness Lengths*; U.S. Army Research Laboratory: Adelphi, MD, USA, 1993.
15. Brutsaert, W. *Evaporation into the Atmosphere: Theory, History and Applications*; Springer: Dordrecht, The Netherlands, 1982; Volume 1.
16. Yang, R.; Friedl, M.A. Determination of roughness lengths for heat and momentum over boreal forests. *Bound.-Layer Meteorol.* **2003**, *107*, 581–603.
17. Ministerio del Ambiente del Ecuador Mapa de Ecosistemas del Ecuador Continental. Available online: http://geoportal.ambiente.gob.ec/portal (accessed on 4 April 2014).
18. Allen, R.G.; Kjaersgaard, J.H.; Garcia, M. Fine-Tuning Components of Inverse-Calibrated, Thermal-Based Remote Sensing Models for Evapotranspiration. In Proceedings of the Pecora 17—The Future of Land Imaging ... Going Operational, Denver, CO, USA, 18–20 November 2008.
19. Paulson, C.A. The mathematical representation of wind speed and temperature profiles in the unstable atmospheric surface layer. *J. Appl. Meteorol.* **1970**, *9*, 857–861.
20. Webb, E.K. Profile relationships: The log-linear range, and extension to strong stability. *Q. J. R. Meteorol. Soc.* **1970**, *96*, 67–90.
21. Allen, R.G.; Tasumi, M.; Morse, A.; Trezza, R.; Wright, J.L.; Bastiaanssen, W.; Kramber, W.; Lorite, I.; Robison, C.W. Satellite-Based Energy Balance for Mapping Evapotranspiration with Internalized Calibration (METRIC)—Applications. *J. Irrig. Drain. Eng.* **2007**, *133*, 395–406.
22. Irmak, A.; Allen, R.G.; Kjaersgaard, J.; Huntington, J.; Kamble, B.; Trezza, R.; Ratcliffe, I.; Kjaersgaard, J.; Huntington, J.; *et al*. Operational Remote Sensing of ET and Challenges. In *Evapotranspiration—Remote Sensing and Modeling*; InTech: Rijeka, Croatia, 2012.
23. Zhu, Z.; Woodcock, C.E. Object-based cloud and cloud shadow detection in Landsat imagery. *Remote Sens. Environ.* **2012**, *118*, 83–94.
24. Kjaersgaard, J.; Richard, A.; Trezza, R.; Robinson, C.; Oliveira, A.; Dhungel, R.; Kra, E. Filling satellite image cloud gaps to create complete images of evapotranspiration. *IAHS Publ.* **2012**, *2012*. 102–105.
25. Allen, R.G.; Trezza, R.; Tasumi, M. Analytical integrated functions for daily solar radiation on slopes. *Agric. For. Meteorol.* **2006**, *139*, 55–73.

26. Kjaersgaard, J.; Allen, R.; Irmak, A. Improved methods for estimating monthly and growing season ET using METRIC applied to moderate resolution satellite imagery. *Hydrol. Process.* **2011**, *25*, 4028–4036.
27. Allen, R.G.; Pereira, L.; Raes, D.; Smith, M. *Crop Evapotranspiration-Guidelines for Computing Crop Water Requirements—FAO Irrigation and Drainage Paper 56*; FAO: Rome, Italy, 1998.